



On the modelling of huge water waves called rogue waves

Christian Kharif

► To cite this version:

Christian Kharif. On the modelling of huge water waves called rogue waves. Anjan Kundu. Tsunami and Nonlinear Waves, Springer Verlag, pp.111-132, 2007, Geo Sciences, 978-3-540-71255-8. 10.1007/978-3-540-71256-5_6 . hal-00458599

HAL Id: hal-00458599

<https://hal.science/hal-00458599>

Submitted on 25 May 2023

HAL is a multi-disciplinary open access archive for the deposit and dissemination of scientific research documents, whether they are published or not. The documents may come from teaching and research institutions in France or abroad, or from public or private research centers.

L'archive ouverte pluridisciplinaire **HAL**, est destinée au dépôt et à la diffusion de documents scientifiques de niveau recherche, publiés ou non, émanant des établissements d'enseignement et de recherche français ou étrangers, des laboratoires publics ou privés.



Distributed under a Creative Commons Attribution| 4.0 International License

On the modelling of huge water waves called rogue waves

Christian Kharif

Institut de Recherche sur les phénomènes Hors Equilibre, Marseille, France

kharif@irphe.univ-mrs.fr

Summary. The chapter focuses on the physics and modelling of the extreme water wave events called rogue waves. A particular attention is paid to their formation in presence of strong wind. Two mechanisms producing the giant waves are considered: The dispersive spatio-temporal focusing and the modulational instability. In both cases an amplification of the height and duration of the rogue wave event is observed under wind action.

1 Introduction

Extreme wave events such as rogue waves correspond to large-amplitude waves occurring suddenly on the sea surface. As it has been emphasized by (13) these huge water waves have been part of marine folklore for centuries. Since the seventies of the last century, oceanographers have started to believe them. In situ observations provided by oil and shipping industries and capsizing of giant vessels confirm the existence of such events. Up to now there is no definitive consensus about a unique definition of rogue wave event. The definition based on height criterion is often used. When the height of the wave exceeds twice the significant height it is considered as a rogue wave. Owing to the non-Gaussian and non-stationary character of the water wave fields on sea surface, it is a very tricky task to compute the probability density function of rogue waves. So, the approaches presented herein are rather deterministic than statistical. Recently (7) and (11) provided reviews on the physics of these events when the direct effect of the wind is not considered. Rogue waves can occur far away from storm areas where wave fields are generated. In that case huge waves are possible on quasi still water. Hence, our approach to the problem is aimed at describing the deterministic mechanisms responsible for the occurrence of these huge waves in presence of strong wind, that is in storm areas.

There are a number of physical mechanisms producing the occurrence of rogue waves. Extreme wave events can be due to refraction (presence of variable currents or bottom topography), dispersion (frequency modulation), wave instability (Benjamin-Feir instability), soliton interactions, etc. that may focus the wave energy into a

small area. All these different mechanisms can work without direct effect of wind on waves. For more details see the paper (11).

The most popular example of rogue waves is that corresponding to abnormal waves appearing suddenly off the south-east coast of South Africa when the dominant wind-generated waves meet a counter-current (Agulhas Current). Theoretical and numerical studies have been developed to understand this wave-current interaction ((23), (12), (26)). Recently, (29) reported experimental results of limiting rogue waves on currents.

Refraction of surface waves can be due to underwater topography as well. The result is spatial variations of the kinematic (frequency and wavenumber) and dynamic (amplitude or energy) properties of the wave packets. The geometrical focusing of wave energy can generate huge waves. Note that rogue waves can arise from wave-current interactions in water of varying depth. It means that refraction effects due to sea bottom and current both are working.

Rogue wave events due to spatio-temporal focusing phenomenon can be described as follows. If initially short wave packets are located in front of longer wave packets having larger group velocities, then during the stage of evolution, longer waves will overtake short waves. A large-amplitude wave can occur at some fixed time because of the superposition of all the waves merging at the same location (the focus point). Afterward, the longer waves will be in front of the short waves, and the amplitude of the wave train will decrease. This focusing-defocusing cycle was described by (18) within the framework of the shallow water theory and later by (22) using the Davey-Stewartson system for three-dimensional water waves propagating in finite depth. More recently, this technique was also used in the experiments on rogue waves conducted by (8) and (25).

Another mechanism generating extreme wave events is the modulational instability or the Benjamin-Feir instability. Due to this instability uniform wave trains suffer modulation-demodulation cycles (the Fermi-Pasta-Ulam recurrence). At the maximum of modulation a frequency downshifting is observed and very steep waves occur.

Soliton interaction as a possible model for extreme waves in shallow water has been suggested by (19) and (20). They considered the interaction of two long-crested shallow water waves within the framework of the two-soliton solution of the Kadomstev-Petviashvili equation. It was found that extreme surface elevation exceeds several times the amplitude of the incoming waves over a small area. In deep water (3) and (4) showed that strong interactions between envelope-solitons may produce rogue wave event. They performed long time simulations based on fully nonlinear equations.

The present study focuses on the two main mechanisms producing rogue waves : The spatio-temporal focusing mechanism and the modulational instability mechanism. In section 2 is defined the criterion which characterizes a rogue wave event. Section 3 presents the equations of water waves and the sheltering theory. The experimental study of extreme wave event is presented in section 4 while section 5 is devoted to the numerical modelling and simulations.

2 Rogue wave definition

In the first approximation, the sea elevation is considered as a summation of sinusoidal waves of different frequencies with random phases and amplitudes. The random wave field is considered as a stationary random Gaussian process with the following probability density distribution

$$f(\eta) = \frac{1}{\sqrt{2\pi}\sigma} \exp\left(-\frac{\eta^2}{2\sigma^2}\right), \quad (1)$$

where η is the sea surface elevation with zero mean level, $\langle \eta \rangle = 0$, and σ^2 is the variance computed from the frequency spectrum, $S(\omega)$

$$\sigma^2 = \langle \eta^2 \rangle = \int_0^\infty S(\omega) d\omega. \quad (2)$$

The wind wave spectrum is assumed to be narrow, thus the cumulative probability function of the wave heights will be given by the Rayleigh distribution

$$P(H) = \exp\left(-\frac{H^2}{8\sigma^2}\right). \quad (3)$$

The probability that the wave heights will exceed a threshold value, H , is given by (3).

One specific wave height frequently used in oceanography and ocean engineering is the significant wave height, H_s . This concept was introduced by (24) who defined H_s as the average of the highest one-third of wave heights. This wave height is close to the mean wave height estimated by human eye. Using the Rayleigh distribution (15) showed that H_s is given by

$$H_s = (3\sqrt{2\pi}\text{erfc}(\sqrt{\ln 3} + 2\sqrt{2\ln 3})\sigma \approx 4\sigma, \quad (4)$$

where $\text{erfc}(\cdot)$ is the complementary error function. So H_s is four times the standard deviation σ . Equation (3) can be rewritten as follows

$$P(H) = \exp\left(-\frac{2H^2}{H_s^2}\right). \quad (5)$$

Mathematically, a wave is considered to be a rogue wave if its height, H_f , satisfies the condition

$$H_f > 2H_s. \quad (6)$$

3 Mathematical formulation

3.1 Water wave equations

The fluid is assumed to be inviscid and the motion irrotational, such that the velocity \mathbf{u} may be expressed as the gradient of a potential $\phi(x, y, z, t)$: $\mathbf{u} = \nabla\phi$. If the fluid is assumed to be incompressible, such that $\nabla \cdot \mathbf{u} = 0$, the equation that holds throughout the fluid is the Laplace's equation

$$\nabla^2 \phi = 0 \quad \text{for} \quad -h < z < \eta(x, y, t). \quad (7)$$

where $\eta(x, y, t)$ is the surface elevation.

The x and y coordinates are taken to be horizontal plane, the z axis vertically upwards. The bottom is located at $z = -h(x, y)$. The bottom condition is

$$\frac{\partial \phi}{\partial x} \frac{\partial h}{\partial x} + \frac{\partial \phi}{\partial y} \frac{\partial h}{\partial y} + \frac{\partial \phi}{\partial z} = 0 \quad \text{on} \quad z = -h(x, y). \quad (8)$$

The kinematic requirement that a particle on the sea surface, $z = \eta(x, y, t)$, remains on it is expressed by

$$\frac{\partial \eta}{\partial t} + \frac{\partial \phi}{\partial x} \frac{\partial \eta}{\partial x} + \frac{\partial \phi}{\partial y} \frac{\partial \eta}{\partial y} - \frac{\partial \phi}{\partial z} = 0 \quad \text{on} \quad z = \eta(x, y, t). \quad (9)$$

Since surface tension effects are ignored, the dynamic boundary condition which corresponds to pressure continuity through the interface, can be written

$$\frac{\partial \phi}{\partial t} + \frac{1}{2}(\nabla \phi)^2 + g\eta + \frac{p_a}{\rho_w} = 0 \quad \text{on} \quad z = \eta(x, y, t). \quad (10)$$

where g is the gravitational acceleration, p_a the pressure at the sea surface and ρ_w the density of the water. The atmospheric pressure at the sea surface can vary in space and time. In water of infinite depth, the kinematic boundary equation (8) is replaced by $\nabla \phi \rightarrow 0$ as $z \rightarrow -\infty$.

The mathematical formulation of the water wave problem has been presented for general 3D flows. The present study is confined to 2D flows and the corresponding equations can be derived from the previous system by using $\partial/\partial y = 0$.

3.2 Wind modelling: The Jeffreys' sheltering theory

Previous works on rogue wave have not considered the direct effect of wind on their dynamics. It was assumed that they occur independently of wind action, that is far away from storm areas where wind wave fields are formed. Herein the Jeffreys' theory (see (9)) is invoked for the modelling of the pressure, p_a . Jeffreys proposed a plausible mechanism to explain the phase shift of the atmospheric pressure, p_a , needed for an energy transfer from wind to the water waves. He suggested that the energy transfer was due to the form drag associated with the flow separation occurring on the leeward side of the crests. The air flow separation would cause a pressure asymmetry with respect to the wave crest resulting in a wave growth. This mechanism can be invoked only if the waves are sufficiently steep to produce air flow separation. (1) have shown that separation occurs over near breaking waves. For weak or moderate steepness of the waves this phenomenon cannot apply and the Jeffreys' sheltering mechanism becomes irrelevant.

Following (9), the pressure at the interface $z = \eta(x, t)$ is related to the local wave slope according to the following expression

$$p_a = \rho_a s (U - c)^2 \frac{\partial \eta}{\partial x}, \quad (11)$$

where the constant, s is termed the sheltering coefficient, U is the wind speed, c is the wave phase velocity and ρ_a is atmospheric density. The sheltering coefficient, $s = 0.5$, has been calculated from experimental data. In order to apply the relation (11) for only very steep waves we introduce a threshold value for the slope $(\partial\eta/\partial x)_c$. When the local slope of the waves becomes larger than this critical value, the pressure is given by equation (11) otherwise the pressure at the interface is taken equal to a constant which is chosen equal to zero without loss of generality. This means that wind forcing is applied locally in time and space. Figure 1¹ shows the pressure distribution at the interface in the vicinity of the crest, given by equation (11), for a threshold value close to the slope corresponding to the Stokes' corner.

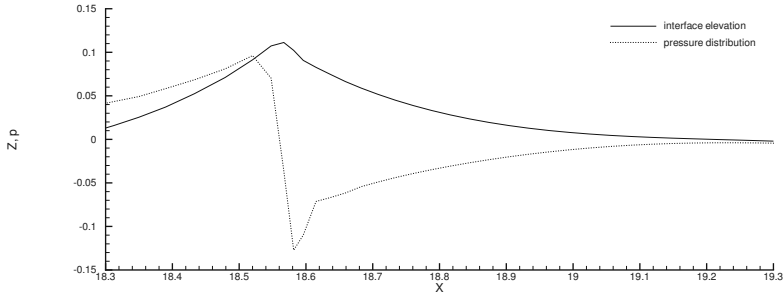


Fig. 1. Pressure at the interface given in 10^{-1} HPa (dotted line) and surface elevation given in m (solid line) as a function of x .

4 Rogue wave observation in presence of wind

Rogue waves have been generated in the large wind-wave tank of IRPHE which is $40m$ long, $1m$ deep and $2.6m$ wide. The wind tunnel above the water surface is $40m$ long, $3.2m$ wide and $1.6m$ high. Figure 2 gives a schematic view of the facility. The blower can produce a wind velocity up to $14m/s$ and a computer-controlled submerged wave maker located under the upstream beach can generate regular or random waves in a frequency range from $0.5Hz$ to $2Hz$. Particular care has been taken to obtain a pure logarithmic mean wind velocity profile with a constant shear layer over the water surface. Several wave gauges are installed on a trolley to measure the water surface elevation at different fetches (distance measured from the upstream beach). For additional details on experiments see the paper by (25)

Rogue waves are generated using the spatio-temporal focusing mechanism based on the dispersive nature of water waves. Within the framework of a linear approach the sea surface can be considered as the superposition of linear waves of frequency

¹ Figures 1, 4, 5 and 6 have been reprinted from (25).

$\omega(x, t)$. According to (28), the spatio-temporal evolution of the frequency of these components is governed by the following hyperbolic equation

$$\frac{\partial \omega}{\partial t} + c_g(\omega) \frac{\partial \omega}{\partial x} = 0, \quad (12)$$

where c_g is the group velocity. This equation can be solved by using the method of characteristics. The solution is given by

$$\omega(x, t) = \omega_0(\tau), \quad v_g(\tau) = c_g(\omega_0(\tau)) \quad \text{on} \quad t = \tau + x/v_g(\tau), \quad (13)$$

where ω_0 corresponds to the temporal frequency distribution of the wave train at $x = 0$. The temporal partial derivative of the frequency is

$$\frac{\partial \omega}{\partial t} = \frac{\frac{d\omega_0}{d\tau}}{1 - \frac{x}{v_g^2} \frac{dv_g}{d\tau}}. \quad (14)$$

One can notice that the case $dv_g/d\tau > 0$, which corresponds to short waves emitted before longer waves, leads to a singularity. This singularity corresponds to the focusing of several waves at $t = T_{f_{th}}$ and $x = X_{f_{th}}$. For infinite depth, the frequency to impose to the wave maker located at $x = 0$ is given by

$$\omega(0, t) = \frac{g}{2} \frac{T_{f_{th}} - t}{X_{f_{th}}}, \quad (15)$$

where $X_{f_{th}}$ and $T_{f_{th}}$ are the coordinates of the point of focus in the $(x - t)$ plane. Using $\omega = 2\pi f$ the coordinates of the focus point reads

$$T_{f_{th}} = \Delta T \frac{f_{\max}}{f_{\max} - f_{\min}}$$

$$X_{f_{th}} = \frac{g\Delta T}{4\pi} \frac{1}{f_{\max} - f_{\min}}$$

where f_{\max} and f_{\min} are the maximal and minimal values of the frequency imposed to the wave maker during a period of time equal to ΔT and g is the acceleration due to gravity.

The wave amplitude, a , satisfies the following equation

$$\frac{\partial a^2}{\partial t} + \frac{\partial}{\partial x}(c_g a^2) = 0. \quad (16)$$

This equation corresponds to the conservation of wave energy, and its solution is found explicitly

$$a(x, t) = \frac{a_0(\tau)}{\sqrt{1 - \frac{x}{v_g^2} \frac{dv_g}{d\tau}}}, \quad (17)$$

where $a_0(\tau)$ is the temporal distribution of the wave amplitude at $x = 0$. Within the framework of the linear theory focus points are singular points where the amplitude becomes infinite and behaves like $(X_{f_{th}} - x)^{-1/2}$.

The wave train generated at the wave maker is uniform in amplitude and frequency modulated. The experimental data are: $f_{\max} = 1.3Hz$, $f_{\min} = 0.8Hz$ and $\Delta T = 10s$. Experiments are performed with and without wind. Figure 3 shows the surface

elevation at a distance of $1m$ from the upstream beach for two values of the wind velocity. It can be seen that the initial group of waves is almost uniform in amplitude and unaffected by wind. From the data we find that $T_{f_{th}} = 26s$ and $X_{f_{th}} = 17m$ while the experimental values are $T_{f_{exp}} = 26s$ and $X_{f_{exp}} = 20m$ (see Figure 4 corresponding to $U = 0m/s$). Experimental data are in close agreement with the linear theory. The difference observed between the theoretical and experimental values of the focus point is mainly due to the nonlinearity of the experimental wave train. Note that the wave train generated at the wave maker is uniform in amplitude, hence the short waves are steeper than the longer waves, and the result is a downstream shift of the focusing location. From Figure 4 it can be seen that dispersion leads short waves to propagate slower than long waves, and as a result, the waves focus at a given position in the wave tank leading to the occurrence of a large amplitude wave. Downstream the point of focus, the amplitude of the group decreases rapidly (defocusing).

The same initial wave train is generated and propagated under the action of wind for several values of the wind velocity ranging from $U = 4m/s$ to $10m/s$ respectively. In presence of wind, the focusing wave train is generated once wind waves have developed. For each value of the mean wind velocity U the water surface elevation is measured at $1m$ fetch and at different fetches between $3m$ and $35m$. The fetch is measured from the entrance of the wave tank where the air flow meets the water surface i.e. at the end of the upstream beach. The wave maker is totally submerged, to avoid any perturbation of the air flow which could be induced by its displacement. Figure 5 shows the same time series of $\eta(x, t)$, at several values of the fetch x , and for a wind speed $U = 6m/s$. The wave groups mechanically generated by the wave maker are identical to those used in the experiments without wind (see Figure 3). Nevertheless, short wind waves can be observed. In any case, some differences appear in the time-space evolution of the focusing wave train. One can observe that the group of the rogue wave event is sustained longer.

The amplification factor $A(x, U)$ of the group between fetches x and $1m$ is defined as follows

$$A(x, U) = \frac{H_{\max}(x, U)}{H_{\text{ref}}}, \quad (18)$$

where U is the mean wind velocity and $H_{\max}(x, U)$ is the maximal height between two consecutive crest and trough in the transient group. The height, H_{ref} , of the quasi uniform wave train generated at the entrance of the tank is measured at $1m$. The mean height crest to trough is $H_{\text{ref}} = 6.13cm$. Figure 6 shows how evolves in space the amplification factor for three values of the wind velocity. For $U = 0m/s$ (without wind) as expected the amplification is maximal at the focus point and the curve exhibits a symmetry with respect to the straight line of equation $x = X_{f_{exp}}$. Focusing and defocusing stages present a symmetrical behaviour. For $U = 4m/s$ and $U = 6m/s$ this symmetry is broken and the focus point is shifted downstream. One can notice that the amplification factor increases as the wind velocity increases. Another important feature is observed: The rogue wave criterion, $A > 2$, is satisfied on a longer distance (or period of time) while the wind velocity increases. The experiments suggest that the physical mechanism which could be responsible of the persistence of rogue events is the occurrence of air flow separation over steep waves.

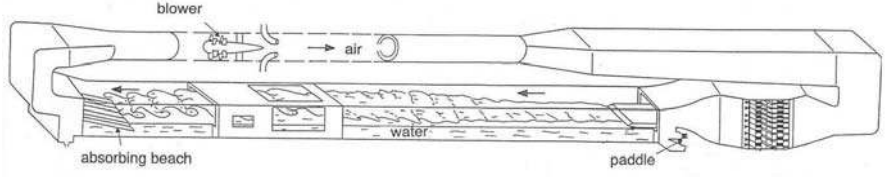


Fig. 2. Schematic view of the wind-wave facility

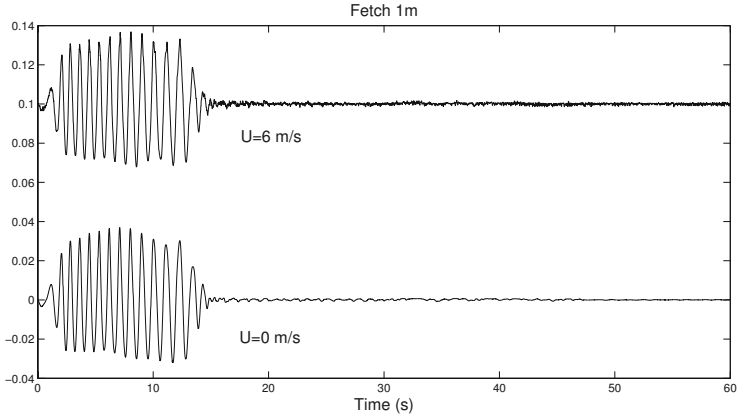


Fig. 3. Surface elevation (in *cm*) at fetch 1*m* for wind velocities $U = 0\text{ m/s}$ and $U = 6\text{ m/s}$.

5 Numerical modelling

5.1 Focusing due to linear dispersion

Herein we considered a numerical wave tank simulating the experimental water wave tank briefly described in the previous section. The gravity wave train is generated by a piston-type wave maker. An absorbing beach located at the end of the wave tank dissipates the incident wave energy.

The Laplace equation (7) is solved within a domain bounded by the water surface and solid boundaries of the numerical wave tank. The condition on the solid boundary writes

$$\nabla \phi \cdot \mathbf{n} = \mathbf{v} \cdot \mathbf{n}, \quad \text{on } \partial\Omega_S, \quad (19)$$

where $\partial\Omega_S$ corresponds to solid boundaries, \mathbf{v} is the velocity of the solid boundaries, set equal to zero on the horizontal bottom and downstream wall of the wave tank and equal to the velocity of the piston at any point of the wave maker, and \mathbf{n} is the unit normal vector to the boundaries.

A Lagrangian description of the water surface is used

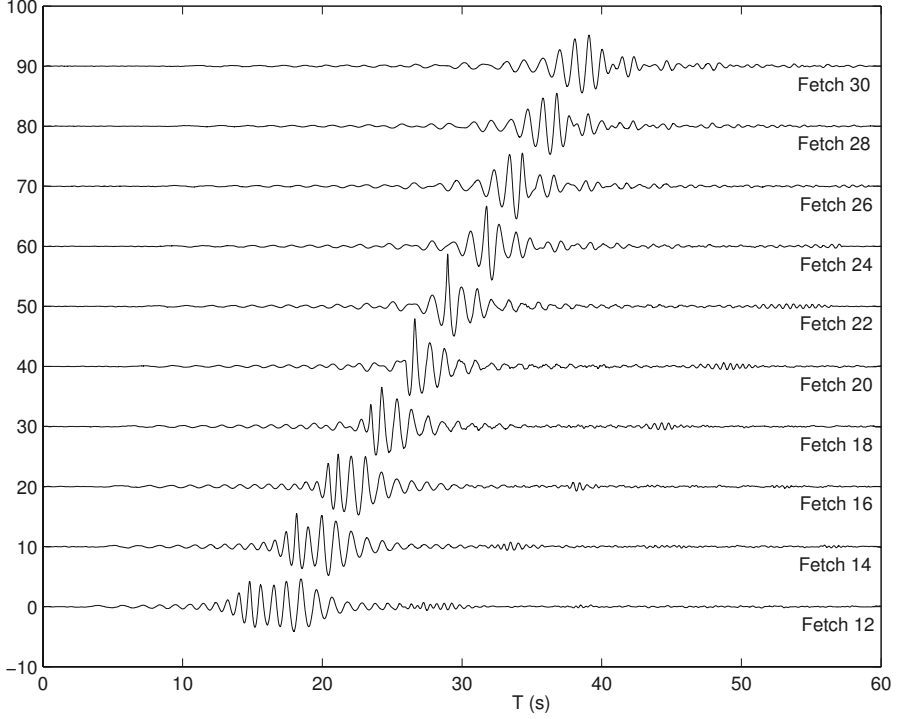


Fig. 4. Surface elevation (in *cm*) at several fetches (in *m*) for wind velocity $U = 0\text{ m/s}$ as a function of time

$$\frac{D\eta}{Dt} = \frac{\partial\phi}{\partial z}, \quad (20)$$

$$\frac{Dx}{Dt} = \frac{\partial\phi}{\partial x}, \quad (21)$$

where x is the abscissa of the water surface and $D/Dt = \partial/\partial t + \nabla\phi \cdot \nabla$.

Equation (20) is an alternative form of equation (9). The kinematic boundary condition writes as well

$$\frac{DS}{Dt} = 0, \quad (22)$$

where $S(x, z, t) = \eta(x, t) - z = 0$ is the water surface equation.

The dynamic boundary condition (10) is rewritten as follows

$$\frac{D\phi}{Dt} = \frac{1}{2}(\nabla\phi)^2 - g\eta - \frac{p_a}{\rho_w}, \quad (23)$$

where the pressure, $p_a(x, t)$, at the water surface is given by equation (11), i.e. the Jeffreys' theory presented in subsection 3.2 is used for modelling wind effect on the extreme waves. Over waves presenting slopes less than a threshold value, the

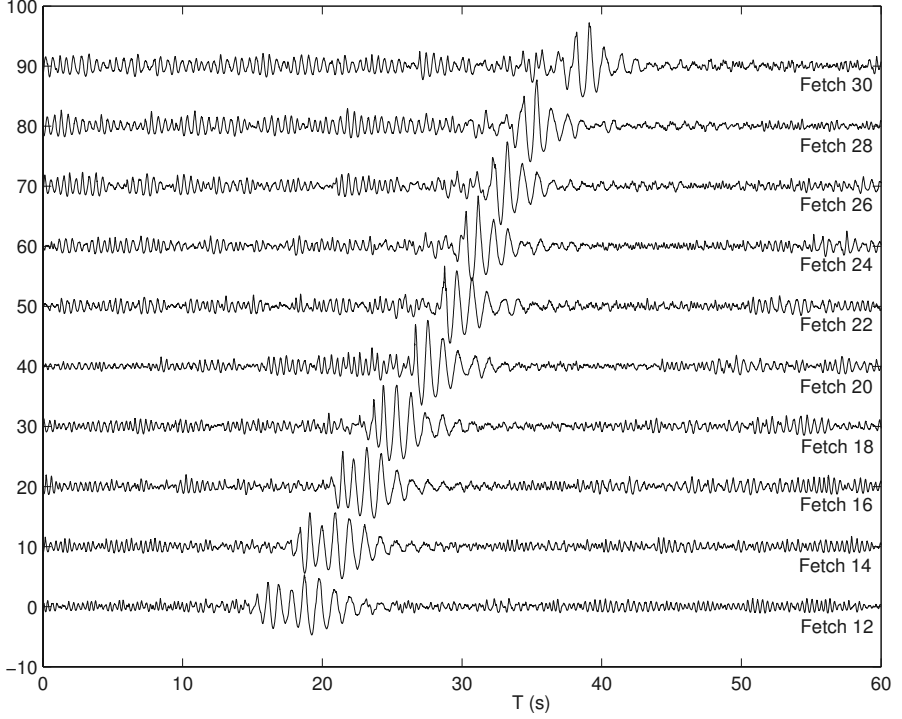


Fig. 5. Surface elevation (in *cm*) at several fetches (in *m*) for wind velocity $U = 6\text{ m/s}$ as a function of time

atmospheric pressure is uniform, set equal to zero without loss of generality.

The system of equations to solve is (7), (19), (20), (21), and (23). The method to integrate numerically this system is a boundary integral equation method (BIEM) with a mixed Euler-Lagrange (MEL) time marching scheme. The numerical method is based on the Green's second identity. For more details see the paper (25).

A focusing wave train is generated by the piston wave maker, leading during the focusing stage to the generation of a extreme wave followed by a defocusing stage. The water surface and the solid boundaries (downstream wall, bottom and wave maker) are discretised by 2000 and 1000 meshes respectively, uniformly distributed. The time integration is performed using a RK4 scheme, with a constant time step of 0.01 s. To avoid numerical instability the grid spacing Δx and time increment Δt have been chosen to satisfy the following Courant criterion derived from the linearized surface conditions

$$(\Delta t)^2 \leq \frac{8\Delta x}{\pi g}. \quad (24)$$

The focusing mechanism is investigated with and without wind as well.

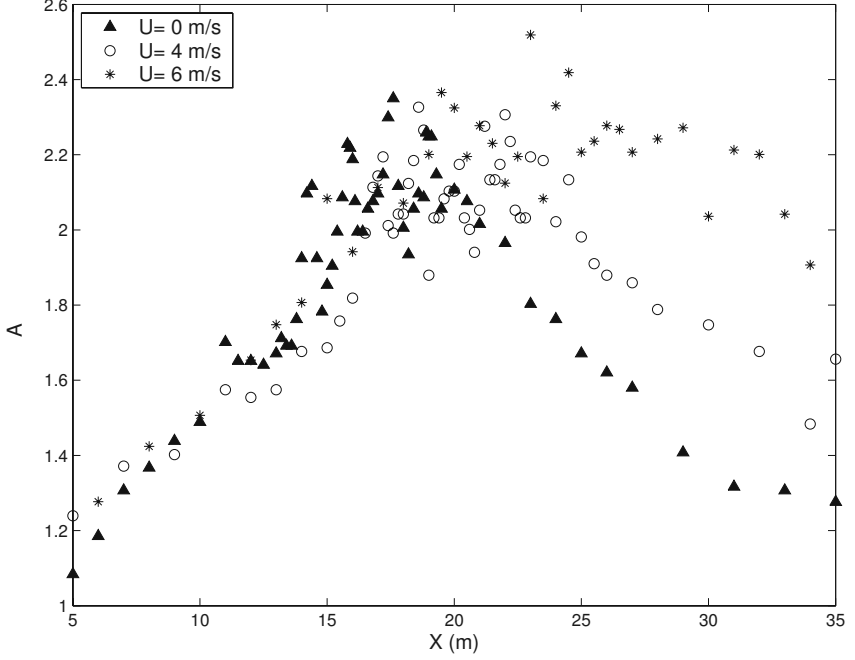


Fig. 6. Experimental amplification factor $A(x, U)$ as a function of the distance (in m) for several values of the wind velocity

A series of numerical simulations have been run for three values of the wind velocity: $U = 0 \text{ m/s}$, 4 m/s , 6 m/s . Using equation (18), Figure 7 describes the spatial evolution of the amplification factor computed numerically. It can be observed that the numerical curves behave similarly to those plotted in Figure 6 and thus emphasize the asymmetry found in the experiments. This asymmetry results in an increase of the life time of the rogue wave event which increases with the wind velocity. The threshold value of the slope beyond which the wind forcing is applied is $(\partial\eta/\partial x)_c = 0.5$. This value corresponds to a wave close to the limiting form for which the Jeffreys' theory applies. Hence the duration of the wind effect is relatively short to increase the amplification of the rogue wave event significantly. However a very weak increase of the amplification factor is observed in presence of wind which is significantly weaker than in the experiments. The main effect of Jeffreys' sheltering mechanism is to sustain the coherence of the short group involving the rogue wave event. Inspection of Figures 6 and 7 shows that the numerical maxima of the amplification factor are larger than those obtained experimentally. This can be due to spilling breaking events which were observed in the experiments, resulting in energy dissipation and in saturation in the growth of amplitude. Notice that the present model which is based on the assumption of inviscid fluid cannot describe energy dissipation. In our model, the transfer of energy from the wind to the water waves depends on the wind velocity and threshold wave slope value. If the latter value is low the energy transferred becomes high and breaking occurs.

To summarize, within the framework of the spatio-temporal focusing both experimental and numerical results are in qualitative good agreement even if some quantitative difference have been observed for the height of the rogue wave.

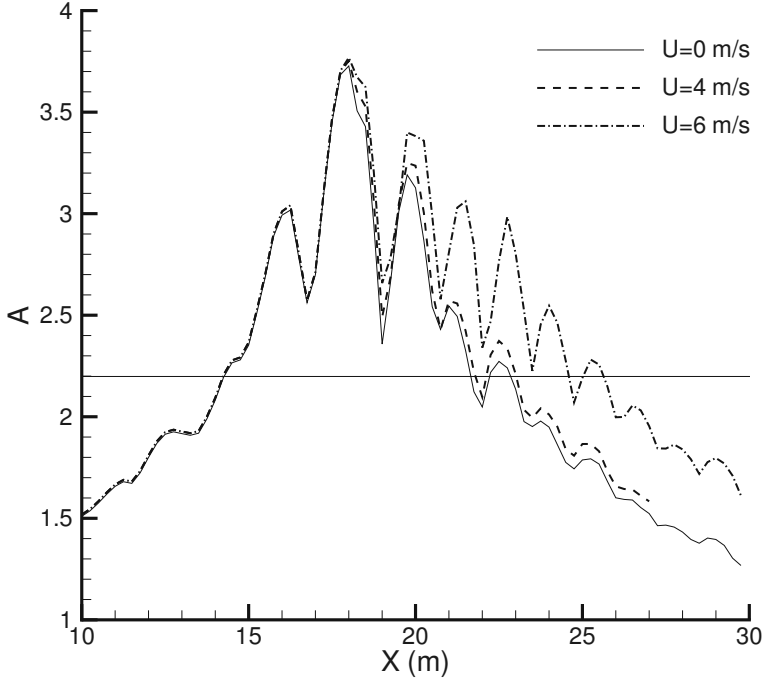


Fig. 7. Numerical amplification factor $A(x, U)$ as a function of the distance (in m) for several values of the wind velocity

5.2 Focusing due to modulational instability

Beside the focusing due to dispersion of a chirped wave group, another mechanism, the modulational instability or Benjamin-Feir instability (see the paper (2)) of uniform wave trains, can generate extreme wave events. This periodic phenomenon is investigated numerically using a high-order spectral method (HOSM) without experimental counterpart. The question is to know how evolve extreme wave events due to modulational instability under strong wind action. How is modified their amplification and time duration under wind effect? Are these effects similar or different from those observed in the case of extreme wave due to dispersive focusing?

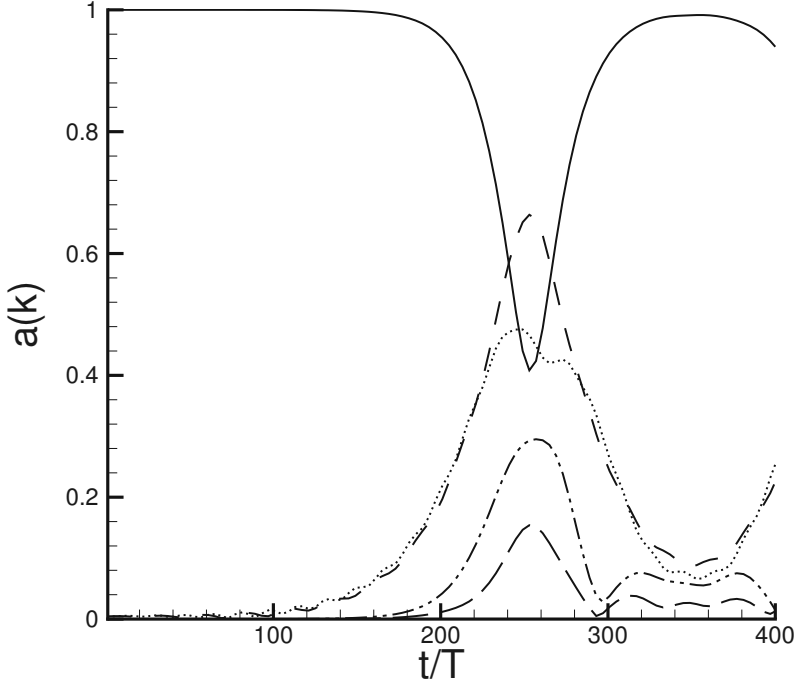


Fig. 8. Time histories of the amplitude of the fundamental, $k_0 = 5$ (solid line), subharmonic, $k_1 = 4$ (dashed line), and superharmonic, $k_2 = 6$ (dotted line), modes for an evolving perturbed Stokes wave of initial wave steepness $\epsilon = 0.11$ and fundamental wave period T , without wind action. The two lowest curves (dashed-dotted lines) correspond to the modes $k_3 = 3$ and $k_4 = 7$.

Introducing the potential velocity at the free surface $\phi^s(x, t) = \phi(x, \eta(x, t), t)$, equations (9) and (10) write

$$\frac{\partial \phi^s}{\partial t} = -\eta - \frac{1}{2} \nabla \phi^s \cdot \nabla \phi^s + \frac{1}{2} W^2 [1 + (\nabla \eta)^2] - p_a, \quad (25)$$

$$\frac{\partial \eta}{\partial t} = -\nabla \phi^s \cdot \nabla \eta + W [1 + (\nabla \eta)^2], \quad (26)$$

where

$$W = \frac{\partial \phi}{\partial z}(x, y, \eta(x, y, t), t). \quad (27)$$

Equations (25) and (26) are given in dimensionless form. Reference length, reference velocity and reference pressure are, $1/k_0$, $\sqrt{g/k_0}$ and $\rho_w g/k_0$ respectively.

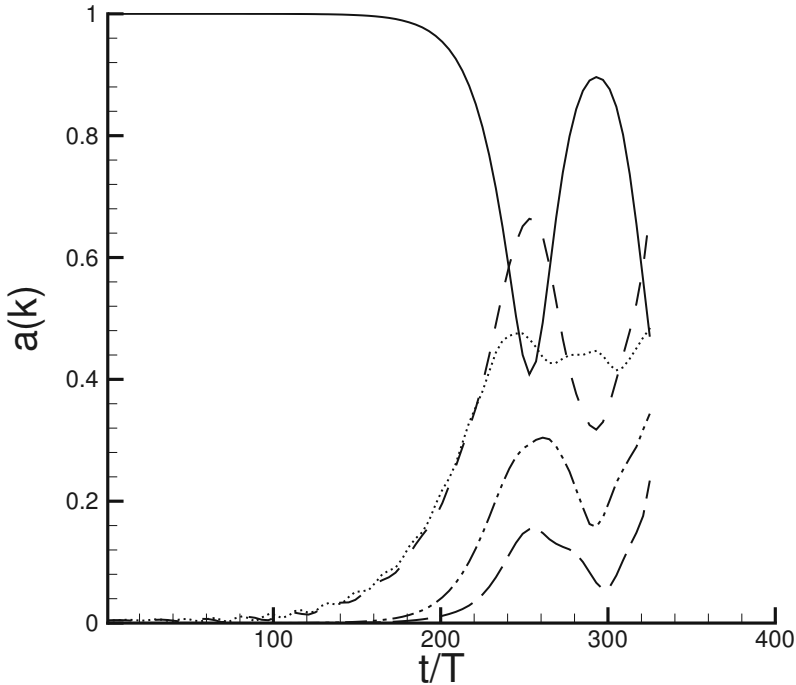


Fig. 9. Time histories of the amplitude of the fundamental, $k_0 = 5$ (solid line), subharmonic, $k_1 = 4$ (dashed line), and superharmonic, $k_2 = 6$ (dotted line), modes for an evolving perturbed Stokes wave of initial wave steepness $\epsilon = 0.11$ and fundamental wave period T , with wind action ($U = 1.75c$). The two lowest curves (dashed-dotted lines) correspond to the modes $k_3 = 3$ and $k_4 = 7$.

The numerical method used to solve the evolution equations is based on a pseudo-spectral treatment with a fourth-order Runge-Kutta integrator with constant time step, similar to the method developed by (6). For more details see the paper (21).

It is well known that uniformly-traveling wave train of Stokes' waves are unstable to the Benjamin-Feir instability (or modulational instability) which results from a quartet resonance, that is, a resonance interaction between four components of the wave field. This instability corresponds to a quartet interaction between the fundamental component (the carrier) $\mathbf{k}_0 = \mathbf{k}_0(1, 0)$ counted twice and two satellites $\mathbf{k}_1 = \mathbf{k}_0(1 + \mathbf{p}, \mathbf{q})$ and $\mathbf{k}_2 = \mathbf{k}_0(1 - \mathbf{p}, -\mathbf{q})$ where p and q are the longitudinal wavenumber and transversal wavenumber respectively of the modulation. Instability occurs when the following resonance conditions are fulfilled.

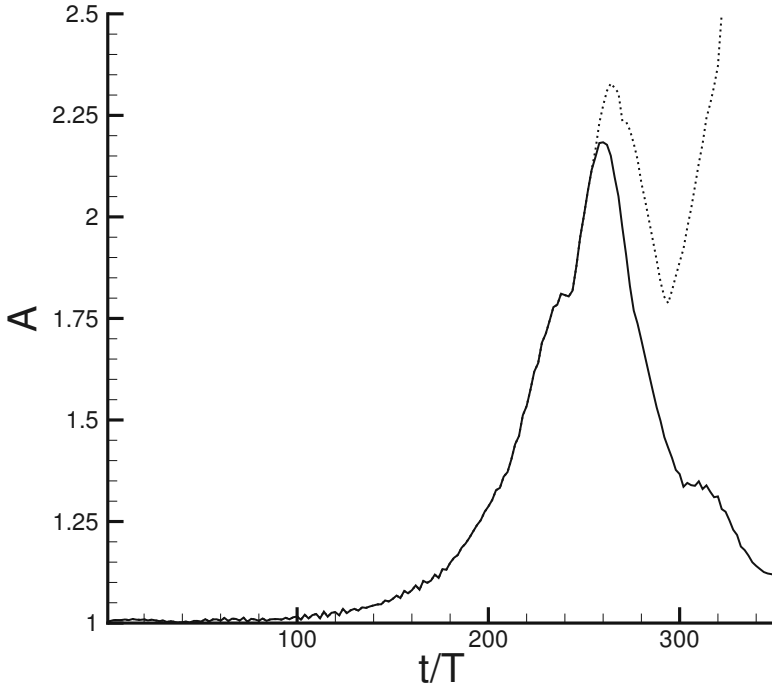


Fig. 10. Numerical amplification factor as a function of time without wind (solid line) and with wind (dotted line) for $U = 1.75c$

$$\mathbf{k}_1 + \mathbf{k}_2 = 2\mathbf{k}_0. \quad (28)$$

$$\omega_1 + \omega_2 = 2\omega_0. \quad (29)$$

where ω_i with $i = 0, 1, 2$ are frequencies of the carrier and satellites.

A presentation of the different classes of instability of Stokes waves is given in the review paper (5).

The procedure used to calculate the linear stability of Stokes waves is similar to the method described by (10). Let $\eta = \bar{\eta} + \eta'$ and $\phi = \bar{\phi} + \phi'$ be the perturbed elevation and perturbed velocity potential where $(\bar{\eta}, \bar{\phi})$ and (η', ϕ') correspond respectively to the unperturbed Stokes wave and infinitesimal perturbative motion ($\eta' \ll \bar{\eta}, \phi' \ll \bar{\phi}$). Following (14), the Stokes wave of amplitude a_0 and wavenumber k_0 is computed iteratively. Substitute these decomposition in the boundary conditions linearized about the unperturbed motion and using the following forms for a two-dimensional flow:

$$\eta' = \exp(\lambda t + i p x) \sum_{-\infty}^{\infty} a_j \exp(i j x), \quad (30)$$

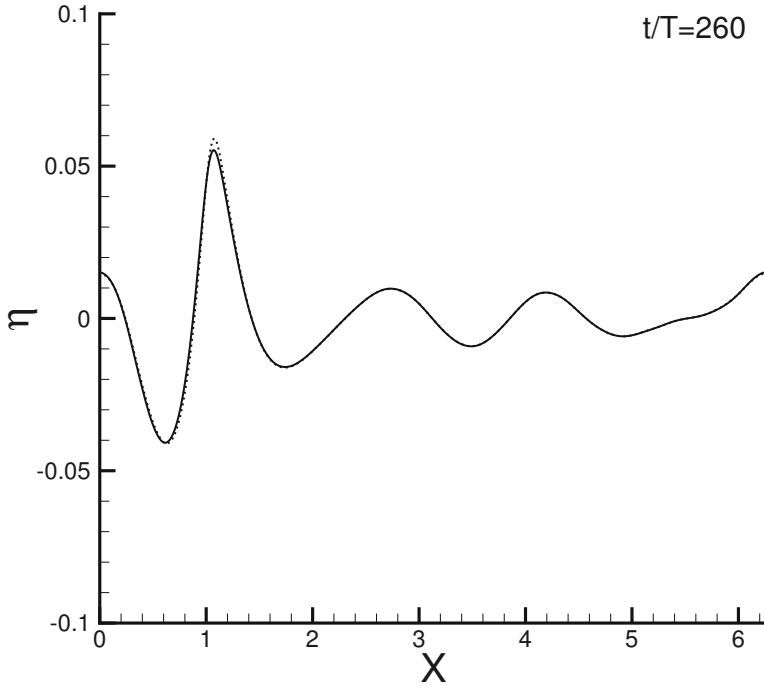


Fig. 11. Surface wave profile at $t = 260T$: without wind (solid line) and with wind (dotted line).

$$\phi' = \exp(\lambda t + ipx) \sum_{-\infty}^{\infty} b_j \exp(ijx + \gamma_j z), \quad (31)$$

where λ , a_j and b_j are complex numbers and $\gamma_j = |p + j|$.

Equations (30) and (31) correspond to an eigenvalue problem for λ with eigenvector $\mathbf{u} = (\mathbf{a}_j, \mathbf{b}_j)^t$:

$$(\mathbf{A} - \lambda \mathbf{B})\mathbf{u} = \mathbf{0}, \quad (32)$$

where \mathbf{A} and \mathbf{B} are complex matrices depending on the unperturbed wave steepness of the basic wave, $\epsilon = a_0 k_0$, and the arbitrary real number p . The eigenvalue, λ , satisfies

$$\det(\lambda \mathbf{B} - \mathbf{A}) = 0. \quad (33)$$

The physical disturbances are obtained from the real part of the complex expressions η' and ϕ' at $t = 0$.

(17) and (16) showed that the dominant instability of a uniformly-traveling train of Stokes' waves in deep water is the two-dimensional modulational instability (class I) provided its steepness is less than $\epsilon = 0.30$. For higher values of the wave steepness

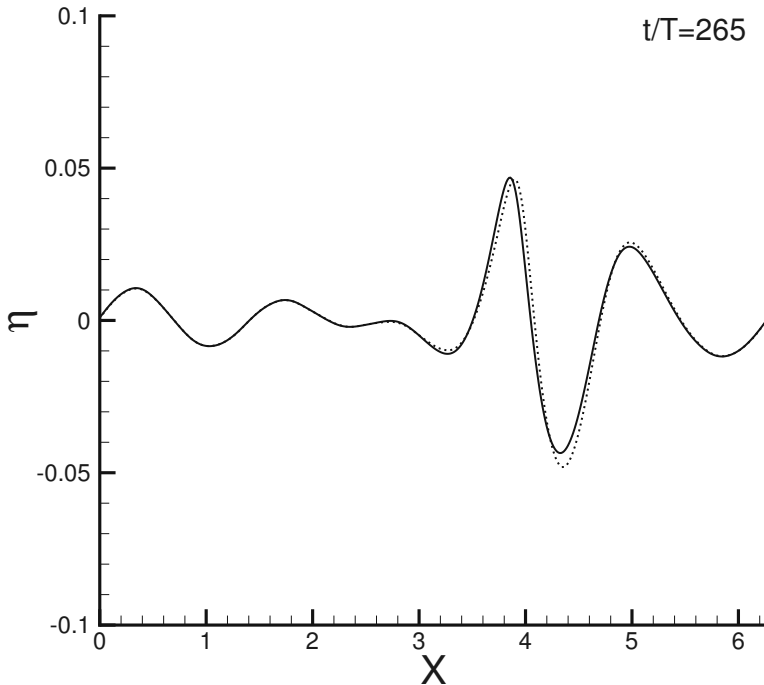


Fig. 12. Surface wave profile at $t = 265T$: without wind (solid line) and with wind (dotted line).

three-dimensional instabilities (class II) become dominant, phase locked to the unperturbed wave. Herein we shall focus on the two-dimensional nonlinear evolution of a Stokes' wave train suffering modulational instability with and without wind action.

Numerical simulation without wind action:

The initial condition is a Stokes wave of steepness $\epsilon = 0.11$, disturbed by its most unstable perturbation which corresponds to $p \approx 0.20 = 1/5$. The fundamental wavenumber of the Stokes wave is chosen so that integral numbers of the sidebands perturbation (satellites) can be fitted into the computational domain. For $p = 1/5$ the fundamental wave harmonic of the Stokes wave is $k_0 = 5$ and the dominant sidebands are $k_1 = 4$ and $k_2 = 6$ for subharmonic and superharmonic part of the perturbation respectively. The wave parameters have been re-scaled in order to have the wavelength of the perturbation equal to 2π . There exists higher harmonics present in the interactions which are not presented here. The normalized amplitude of the perturbation relative to Stokes wave amplitude is initially taken

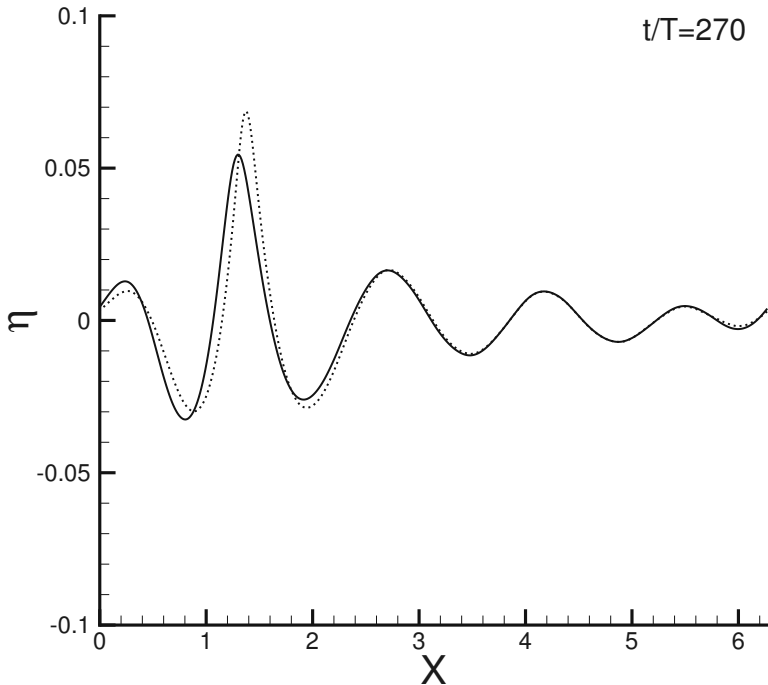


Fig. 13. Surface wave profile at $t = 270T$: without wind (solid line) and with wind (dotted line).

equal to 10^{-3} . The order of nonlinearity is $M = 6$, the number of mesh points is $N > (M + 1)k_{\max}$ where k_{\max} is the highest harmonic taken into account in the simulation. The latter criterion concerning N is introduced to avoid aliasing errors. To compute the long time evolution of the wave packet the time step Δt is chosen equal to $T/100$ where T is the fundamental period of the basic wave. This temporal discretisation satisfies the CFL condition.

For the case without wind, the time histories of the normalized amplitude of the carrier, lower sideband and upper sideband of the most unstable perturbation are plotted in Figure 8. Another perturbation which was initially linearly stable becomes unstable in the vicinity of maximum of modulation resulting in the growth of the sidebands $k_3 = 3$ and $k_4 = 7$. The nonlinear evolution of the two-dimensional wave train exhibits the Fermi-Pasta-Ulam recurrence phenomenon. This phenomenon is characterized by a series of modulation-demodulation cycles in which initially uniform wave trains become modulated and then demodulated until they are again uniform. Herein one cycle is reported. At $t \approx 360T$ the initial condition is more or less recovered. At the maximum of modulation $t = 260T$, one can observe a temporary frequency (and wavenumber) downshifting since the subharmonic mode $k_1 = 4$

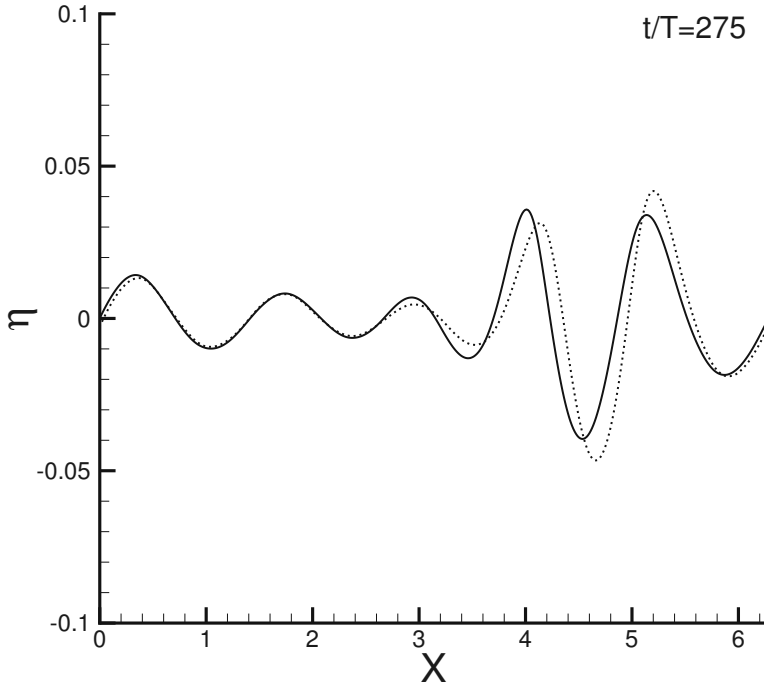


Fig. 14. Surface wave profile at $t = 275T$: without wind (solid line) and with wind (dotted line).

is dominant. At this stage a very steep wave occurs in the group as it can be seen in Figure 11.

Numerical simulation with wind action:

Figure 9 is similar to Figure 8, except that now water waves evolve under wind action. Wind forcing is applied over crests of slopes larger than $(\partial\eta/\partial x)_c = 0.405$. This condition is satisfied for $256T < t < 270T$, that is during the maximum of modulation which corresponds to the formation of the extreme wave event. When the values of the wind velocity are too high numerical simulations fail during the formation of the rogue wave event, due to breaking. During breaking wave process the slope of the surface becomes infinite, leading numerically to a spread of energy into high wavenumbers. This local steepening is characterized by a numerical blow-up (for methods dealing with an Eulerian description of the flow). In order to avoid a breaking wave too early, the wind velocity is fixed $U \approx 1.75c$. Owing to the weak

effect of the wind on the phase velocity of the crests on which it acts, the phase velocity, c , is computed without wind. The effect of the wind reduces significantly the demodulation cycle and thus sustains the rogue wave event. This feature is clearly shown in Figure 10. The amplification factor is stronger in presence of wind and the rogue wave criterion given by equation (6), $A > 2$, is satisfied during a longer period of time. Figures 11, 12, 13 and 14 display water wave profiles at different instant of time in the vicinity of the maximum of modulation with and without wind. The solid lines correspond to waves propagating without wind while the dotted lines represent the wave profiles under wind action. These figures show that the wind does not modify the phase velocity of the very steep waves while it increases their height.

To summarize the results of this section, we can claim that extreme wave events generated by modulational instability in presence of wind behave similarly to those due to dispersive spatio-temporal focusing discussed in previous section 4 and subsection 5.1.

6 Conclusion

Two main mechanisms yielding to rogue wave events have been investigated experimentally and numerically. Within the framework of extreme wave events due to spatio-temporal focusing a good qualitative agreement is found between experiments and numerical simulations. It is shown that the wind amplifies the height of the steep waves and increases their duration. A second series of numerical simulations have been performed within the framework of rogue waves due to modulational instability. For this case no experiments have been conducted. Nevertheless the simulations have confirmed the results found for extreme wave events due to the spatio-temporal focusing phenomenon.

References

- [1] M. I. Banner and W.K. Melville (1976) On the separation of air flow over water waves, *J. Fluid Mech.* 77, 825–842.
- [2] T.B. Benjamin and J.E. Feir 1967 The desintegration of wave trains on deep water. Part 1. Theory., *J. Fluid Mech.* 27, 417–430.
- [3] D. Clamond and J. Grue (2002) Interaction between envelope solitons as a model for freak wave formation. Pt 1: Long-time interaction, *C.R. Mecanique* 330, 575–580.
- [4] D. Clamond, M. Francius, J. Grue and C. Kharif (2006) Strong interaction between envelope solitary surface gravity waves, *Eur. J. Mech. B/Fluids*, 25(5), 536–553.
- [5] F.Dias and C. Kharif (1999) Nonlinear gravity and capillary-gravity waves, *Annu. Rev. Fluid Mech.* 31, 301–346.
- [6] D.G. Dommermuth and D.K.P. Yue (1987) A high-order spectral method for the study of nonlinear gravity waves, *J. Fluid Mech.* 184, 267–288.
- [7] K.B. Dysthe (2001) Modelling a "Rogue Wave" - Speculations or a realistic possibility?, *Rogues Waves 2000* edited by M. Olagnon and G.A. Athanassoulis (Brest, France), 255–264, 2001.
- [8] J.P. Giovanangeli, C. Kharif and E. Pelinovsky (2004) Experimental study of the wind effect on the focusing of transient wave groups, *Proc. of abstracts of Rogue waves 2004*, Brest.
- [9] H. Jeffreys (1925) On the formation of wave by wind , *Proc. Roy. Soc. A* 107, 189–206.
- [10] C. Kharif and A. Ramamonjisoa (1988) Deep water gravity wave instabilities at large steepness, *Phys. Fluids* 31, 1286–1288.
- [11] C. Kharif and E. Pelinovsky (2003) Physical mechanisms of the rogue wave phenomenon, *Eur. J. Mech. B/Fluids* 22, 603–634.
- [12] I.V. Lavranov (1998) The wave energy concentration at the Agulhas current off South Africa, *Natural Hazards* 17, 117–127.
- [13] G. Lawton (2001) Monsters of the deep (The perfect wave), *New Scientist* 170 (2297), 28–32.
- [14] M.S. Longuet-Higgins (1985) Bifurcation in gravity waves, *J. Fluid Mech.* 151, 457–475.
- [15] S.R. Massel (1996) *Ocean surface waves: Their physics and prediction*, World Scientific, Singapour.
- [16] J.W. McLean (1982) Instabilities of finite-amplitude water waves, *J. Fluid Mech.* 114, 315–330.
- [17] J.W. McLean, Y.C. Ma, D.U. Martin, P.G. Saffman and H.C. Yuen (1981) Three-dimensional instability of finite-amplitude water waves, *Phys. Rev. Lett.* 46, 817–820.
- [18] E. Pelinovsky, T. Talipova and C. Kharif (2000) Nonlinear dispersive mechanism of the freak wave formation in shallow water, *Physica D* 147(1-2), 83–94.
- [19] P. Peterson, T. Soomere, J. Engelbrecht and E. van Groesen (2003) Soliton interaction as a possible model for extreme waves, *Nonlinear Processes in Geophysics* 10, 503–510.
- [20] T. Soomere and J. Engelbrecht (2005) Extreme elevations and slopes of interacting solitons in shallow water, *Wave Motion* 41, 179–192.

- [21] C. Skandrani, C. Kharif and J. Poitevin (1996) Nonlinear evolution of water surface waves: The frequency downshifting phenomenon, *Contemp. Math.* 200, 157–171.
- [22] A. Slunyaev, C. Kharif, E. Pelinovsky and T. Talipova (2002) Nonlinear wave focusing on water of finite depth, *Physica D* 173(1-2), 77–96.
- [23] R. Smith (1976) Giant waves, *J. Fluid Mech.* 77, 417–431.
- [24] H.U. Sverdrup and W.H. Munk (1947) Wind, sea, and swell; theory of relations for forecasting, U.S. Navy Hydrographic Office, H.O. 601.
- [25] J. Touboul, J.P. Giovanangeli, C. Kharif and E. Pelinovsky (2006) Freak waves under the action of wind: Experiments and simulations, *Eur. J. Mech. B/Fluids* 25, 662–676.
- [26] B.S. White and B. Fornberg (1998) On the chance of freak waves at the sea, *J. Fluid Mech.* 255, 113–138.
- [27] G.B. Whitham (1965) A general approach to linear and non-linear dispersive waves using a Lagrangian, *J. Fluid Mech.* 22, 273–283.
- [28] G.B. Whitham (1967) Nonlinear dispersion of water waves, *J. Fluid Mech.* 27, 399–412.
- [29] C.H. Wu and A. Yao (2004) Laboratory measurements of limiting freak waves on currents, *J. Geophys. Res.* 109, C12002, 1–18.